Supplementary Information (SI) for Green Chemistry.

Supplementary Information

Asymmetric defective sites-triggered triple synergistic modulation in nanoconfined-aerogel for superior electrochemical low-concentration nitrate-to-ammonia

Ke Wang[a] , Tong Zhao [a], Shiyu Zhang [a], Rupeng Wang [a], Meng Wang [a], Zixiang He [a], Shih-Hsin Ho [a]*

[a]State Key Laboratory of Urban Water Resource and Environment, School of Environment, Harbin Institute of Technology, Harbin, 150090, P. R. China.

*Corresponding author. E-mail: stephen6949@msn.com

Supplementary Experiments

Text S1. Chemicals

Cobalt acetate tetrahydrate ($Co(CH_3COO)_2 \cdot 4H_2O$, 99%), 2-methylimidazole (2-mIM, 98%), carboxymethyl cellulose (CMC, AR), potassium hydroxide (NaOH, AR), sodium nitrate ($Na^{14}NO_3$, 99.99%), sodium nitrate ($Na^{15}NO_3$, 98.5%), sodium nitrite ($NaNO_2$, 99.99%), sodium sulfate (Na_2SO_4, 99%), sodium citrate ($C_6H_5O_7Na_3$, 98%), salicylic acid ($C_7H_6O_3$, 99.5%), sodium nitroferricyanide dihydrate ($C_5FeN_6Na_2O.2H_2O$ 99.0%), sodium chloride (NaCl, 99.99%), sodium bicarbonate ($NaHCO_3$, 99%), sodium carbonate (Na_2CO_3, 99%), Humic acid (HA, 90%), calcium sulfate ($CaSO_4$, AR), and magnesium sulfate ($MgSO_4$, AR) were purchased from Aladdin Reagent Co., Ltd. (Shanghai, China). Hydrochloric acid (HCl, AR) was purchased from Sinopharm Chemical Reagent Co., Ltd. (Shanghai, China). Sulfanilamide ($C_6H_8N_2O_2S$, 99.5%), N-(1-naphthyl) ethylenediamine dihydrochloride ($C_{12}H_{14}N_2 \cdot 2HCl$, >98%), sulfamic acid ($H_3NO_3S$, 99.5%), phosphoric acid (H_3PO_4, AR), sodium hypochlorite (NaClO, AR), cobalt powder (20-30 nm, 99.9%), tert-Butanol (TBA, 99%), and ammonium chloride (NH_4Cl, 99.99%) were purchased from Macklin Biochemical Co., Ltd. (Shanghai, China). Spirulina-based reduced graphene oxide (SRGO) was prepared according to our previous works after ascorbic acid reduction [1]. All chemicals were analytical grade and used without further purification.

Text S2. Characterization methods

The morphological characteristics and microstructures of the samples were observed by field-emission scanning electron microscopy (SEM, Hitachi S-4800, Japan) and field-emission transmission electron microscopy (TEM, JEOL-2001F), while the crystalline structures were obtained by X-ray diffraction using Cu Kα irradiation (XRD, Bruker D8, Germany). The chemical compositions and the valence of the elements in the samples were investigated by X-ray photoelectron spectroscopy using an Al-Kα X-ray source (XPS, Thermo Escalab 250, America). The isotope labeling experiments were measured by ^{1}H-NMR measurement (Bruker 600-MHz, Germany). The Raman spectra were obtained Via Raman spectroscopy system (Renishaw, UK) with a 532-nm excitation laser to determine the degree of graphitization of the prepared materials. The concentrations of nitrogen species were determined through ultraviolet–visible (UV–vis) spectrophotometer (UV-6000, China). The measurement of oxygen vacancies in the sample was conducted using an EPR spectrometer (Bruker A300, Germany). The specific surface area was calculated based on the Brunauer-Emmett-Teller equation (BET, NOVA2000E. America) in the pressure P/Po range. The hydrophilicity was tested by a contact angle instrument (CA, Dataphysics OCA 20, Germany). The Work function was tested by Scanning Kelvin probe (SKP) (SKP5050 system, Scotland). Inductively coupled plasma mass spectrometer (ICP-MS, PerkinElmer NexION 300X, America) was used to determine the Co_3O_4 loading.

Text S3. Determination of nitrogen species concentration

The ion concentration was quantified by the UV-Vis spectrophotometer, after diluting to an appropriate concentration based on the calibration curves. The specific detection methods are as follows:

NO_3^--N quantification. First, 0.2 mL of the electrolyte after the electrochemical nitrate reduction reaction test was diluted to 5 mL with water, then 0.1 mL of HCl solution (1 M) and 0.01 mL of 0.8 wt% sulfamic acid solution were added, and the color was developed for 10 min. Subsequently, the absorbance was measured by UV-vis spectrophotometry in the wavelength of 220 nm and 275 nm. Nitrate-N final absorbance was obtained from the following equation: $A = A_{220nm} - 2A_{275nm}$. The concentration-absorbance calibration curve was plotted using a series of concentration known standard $NaNO_3$ solutions dissolved in 0.1 M Na_2SO_4.

NO_2^--N quantification. The concentration of NO_2^- was determined by Griess method. The color agent was prepared as follows: 50 mL deionized water and 10 mL phosphoric acid were mixed together, followed by adding 4.0 g sulfanilamide and 0.2 g of N-(1-naphthyl)-ethylenediamine 5 dihydrochloride. The mixture was then diluted to calibration tail in a 100 mL volumetric flask. In addition to that, 5 mL electrolyte diluted to the detection range was taken out into a test tube, followed by adding 0.1 mL color reagent. After shaking and standing for 20 min, the absorbance value at a wavelength of 540 nm was recorded by UV-Vis absorption spectra. The concentration-absorbance calibration curve was plotted using a series of concentration known standard $NaNO_2$ solutions dissolved in 0.1 M Na_2SO_4.

NH_3-N quantification. The concentration of NH_3 was determined by the indophenol blue method. Specifically, a certain amount of electrolyte was extracted out to dilute to the detection range. And then 2 mL diluted electrolyte was taken out into a test tube, followed by adding 2 mL 1.0 M NaOH solution containing 5.0 wt% salicylic acid ($C_7H_6O_3$) and 5.0 wt% sodium citrates ($C_6H_5Na_3O_7 \cdot 2H_2O$), 1 mL NaClO (0.05 M) solution and 0.2 mL 1.0 wt% sodium nitroferricyanide ($Na_2[Fe(NO)(CN)_5] \cdot 2H_2O$) solution. After standing for 2 h in dark place under ambient conditions, UV-Vis absorption spectra were measured, and the absorbance value at a wavelength of 655 nm was collected. In order to quantify the concentration, the concentration-absorbance calibration curve was plotted using a series of standard NH_4Cl solutions dissolved in 0.1 M Na_2SO_4.

Text S4. Calculation of the NO_3RR parameters

The NO_3^--N conversion was calculated as follow:

$$NO_3^-\text{-N conversion (\%)} = \Delta c_{NO_3^-\text{-N}}/c_0 \times 100\%$$

The selectivity of NH_3-N was calculated as follow:

$$NH_3\text{-N selectivity (\%)} = c_{NH_3\text{-N}}/\Delta c_{NO_3^-\text{-N}} \times 100\%$$

The Faradaic efficiency was calculated as follow:

$$FE_{NH_3\text{-N}}\ (\%) = 8 \times F \times c_{NH_3\text{-N}} \times V/17 \times Q$$

The yield rate of NH_3-N was calculated as follow:

$$NH_3\text{-N yield (mg h}^{-1}\text{ cm}^{-2}) = c_{NH_3\text{-N}} \times V/t \times S$$

where $c_{NH_3\text{-N}}$ is the mass concentration of NH_3-N(mg/L), V is the volume of electrolyte in the cathode compartment (mL), M is the molar mass of NH_3, t is the electrolysis time (h), S is the geometric area of working electrode (cm^2), $\Delta c_{NO_3^-\text{-N}}$ is the concentration difference of NO_3^--N before and after electrolysis, c_0 is the initial concentration of NO_3^--N, F is the Faradaic constant (96485 C mol^{-1}), Q is the total charge passing the electrode.

Text S5. *In-situ* FT-IR measurements

In situ Fourier transformed infrared spectroscopy (FT-IR) were obtained on a Bruker INVENIO S spectrometer. A thin gold film was chemically deposited on the surface of a silicon crystal. The ink of the sample was dropped on the aforementioned gold film supported by silicon, and the whole was served as the working electrode. Platinum foil and Ag/AgCl electrodes were used as the counter electrode and the reference electrode, respectively. 140 mg/L NO_3^--N with 0.1 M Na_2SO_4 electrolyte were used as the reactant. LSV curves were conducted from 0.0 V to -1 V vs. RHE. with a scan rate of 10 mV s^{-1}.

Text S6. Online DEMS measurements

The mass spectrometer and an electrochemical workstation were used for the online differential electrochemical mass spectrometry (DEMS) measurements. 140 mg/L NO_3^--N with 0.1 M Na_2SO_4 electrolyte was prepared as the electrolyte. Ar was bubbled into the electrolyte constantly before and during the DEMS measurements. The as-prepared sample, Pt wire, and Ag/AgCl electrode were used as the working electrode, counter electrode, and reference electrode, respectively. Potentiostatic test at -0.8 V vs. RHE was performed and the corresponding mass signals can be detected during this period. After the electrochemical test was over and the mass signal returned to baseline, the next cycle was started using the same test conditions to avoid the accidental error during DEMS measurements. The measurement was ended after three cycles.

Text S7. FEM simulations

The COMSOL Multiphysics software package was used to conduct FEM simulations. Based on the experimental data, the diameter of Co_3O_4 nanoparticles (blue semicircle) was determined to be 20 nm, and the pore diameter of porous SRGA (gray shell) was determined to be 4 nm. The solution of 0.1 M Na_2SO_4 with 10 mM NO_3^--N was allowed to diffuse to the surface of catalysts. The “Chemistry” module defined surface equilibrium reactions on the porous carbon shell for the adsorption-desorption of NO_3^-, while the “Transport of Diluted Species” module was utilized to model the diffusion of NO_3^-.

Text S8. DFT computational details

The Co_3O_4 surface was modeled using a periodic slab structure with lattice parameters of a = 12.0014 Å, b = 12.2345 Å, and c = 20.0000 Å, including a vacuum layer of 15 Å along the c-axis to eliminate inter-slab interactions. A surface oxygen atom was deliberately removed to introduce oxygen vacancies, simulating surface defect states that are typically present in catalytic conditions. This defect model allows for the investigation of the role of surface oxygen vacancies in modulating adsorption properties and electronic structure.

First-principles calculations were performed within the density functional theory framework. The projector-augmented wave (PAW) method [2] and the generalized gradient approximation (GGA) [3] for the exchange-correlation energy functional, as implemented in the Vienna ab initio simulation package (VASP) were used [4]. The GGA calculation was conducted with the Perdew-Burke-Ernzerhof (PBE) exchange-correlation potential [5]. Considering long-range interaction between molecules/intermediates and surface, Van der Waals interactions were considered using DFT-D3 correlation. A slab model of 1×1×1 conventional cell of Co_3O_4 surface with six atomic layers as used to model the catalyst. To avoid effects from other slabs, a vacuum of 15 Å was added along z direction. The convergence criterion of geometry relaxation was set to 0.03 eV·Å in force on each atom. The energy cutoff for the plane wave-basis was set to 500 eV. The K points were sampled with 3×3×1 by the Monkhorst-Pack method. The change in free energy (ΔG) of per reaction step was calculated as follows,

$$\Delta G = \Delta E + \Delta ZPE - T\Delta S$$

where ΔE is the change of the total reaction energy obtained from DFT calculation, ΔZPE the change of the zero-point energy, T the temperature (300 K), and ΔS the change of the entropy.

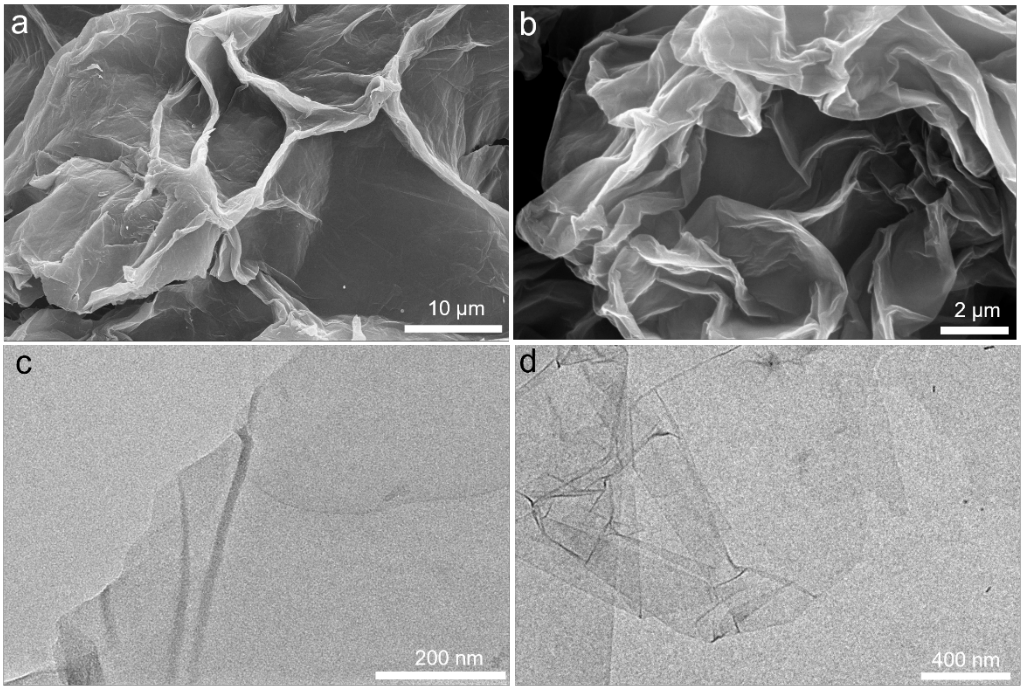

Figure S1. (a, b) SEM images and (c, d) TEM images of SRGO.

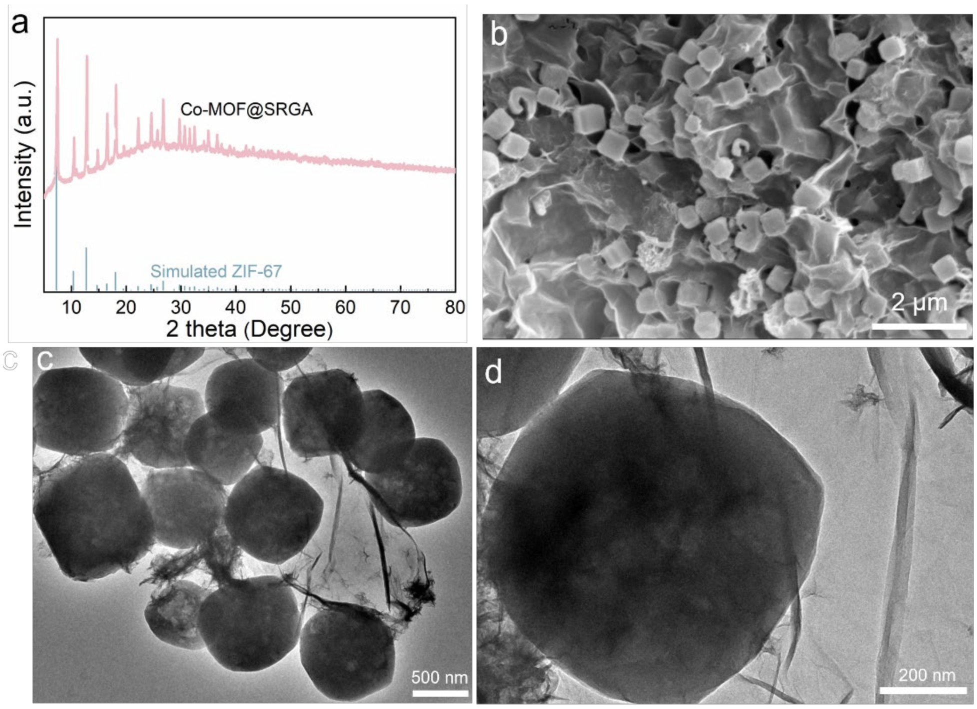

Figure S2. (a) XRD patterns, (b) SEM images and (c, d) TEM images of Co-MOF/SRGA.

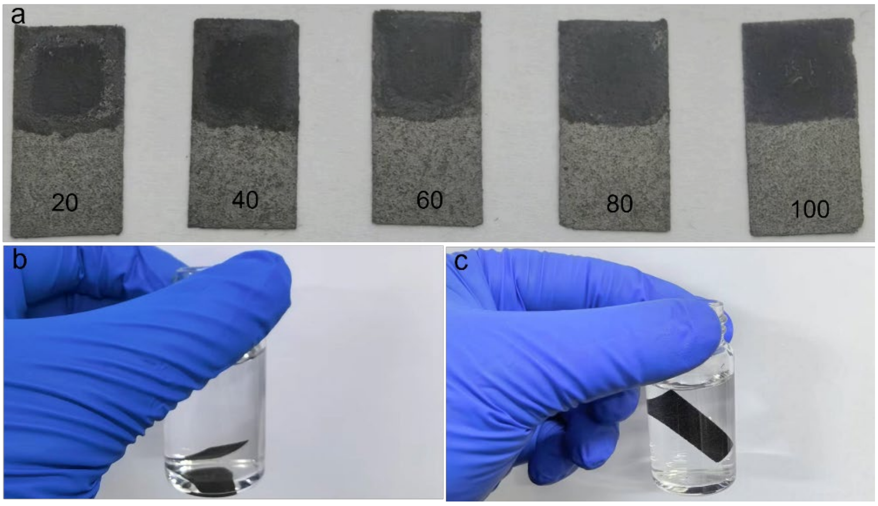

Figure S3. (a) Photos of Vo-HCo_3O_4@SRGA on carbon paper with different mass loadings. photographs of Vo-HCo_3O_4@SRGA-80 (b) before and (c) after 200 h of immersion in the electrolyte.

When the coating amounts of Co-MOF@SRGO hydrogels was 80 μL, the best stability was maintained while maximizing the uniform distribution of Vo-HCo_3O_4@SRGA on the surface of carbon paper. Since the loading amount is too low, Vo-HCo_3O_4@SRGA cannot completely cover the surface of carbon paper, and when the loading amount is too high, it leads to the cracking of Vo-HCo_3O_4@SRGA on the surface and decreases the stability. Vo-HCo_3O_4@SRGA shows no significant shedding even after 200 hours of immersion in electrolyte, indicating its excellent stability.

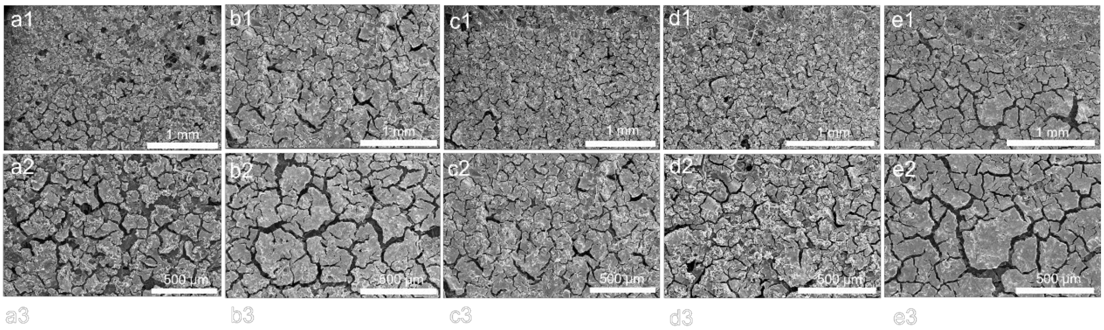

Figure S4. SEM images of (a) Vo-HCo$_3$O$_4$@SRGA-20, (b) Vo-HCo$_3$O$_4$@SRGA-40, (c) Vo-HCo$_3$O$_4$@SRGA-60, (d) Vo-HCo$_3$O$_4$@SRGA-80, and Vo-HCo$_3$O$_4$@SRGA-100 on carbon paper.

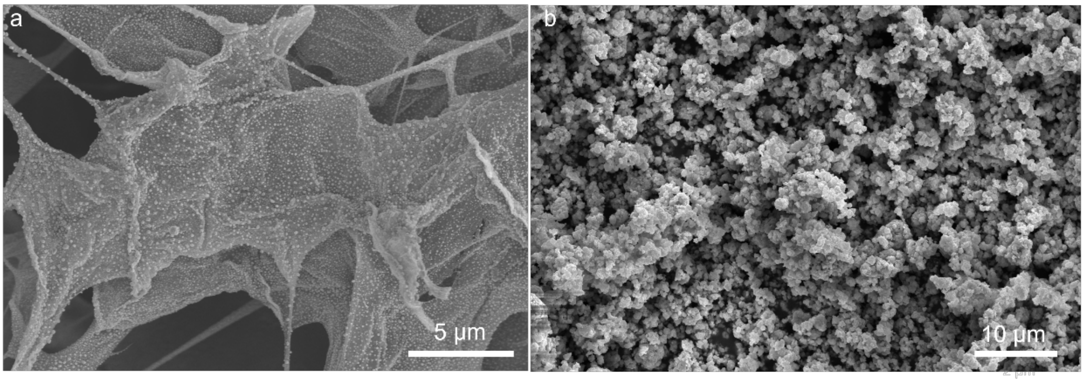

Figure S5. SEM images of (a)Vo-HCo_3O_4@SRGA and (b) Vo-HCo_3O_4.

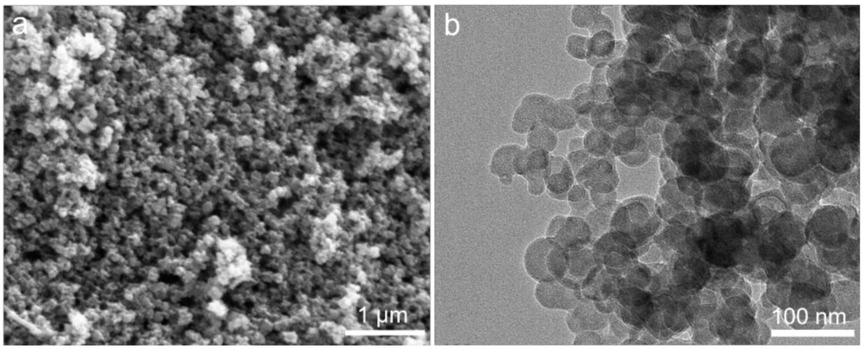

Figure S6. (a) SEM and (b) TEM images of H-Co_3O_4.

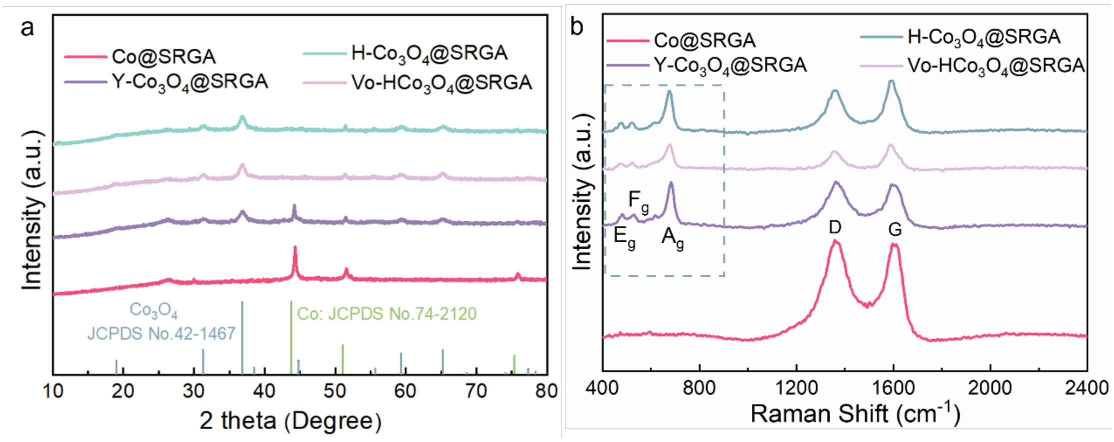

Figure S7. (a) XRD and (b) Raman spectra of Co@SRGA, H-Co$_3$O$_4$@SRGA, Y-Co$_3$O$_4$@SRGA, and Vo-HCo$_3$O$_4$@SRGA.

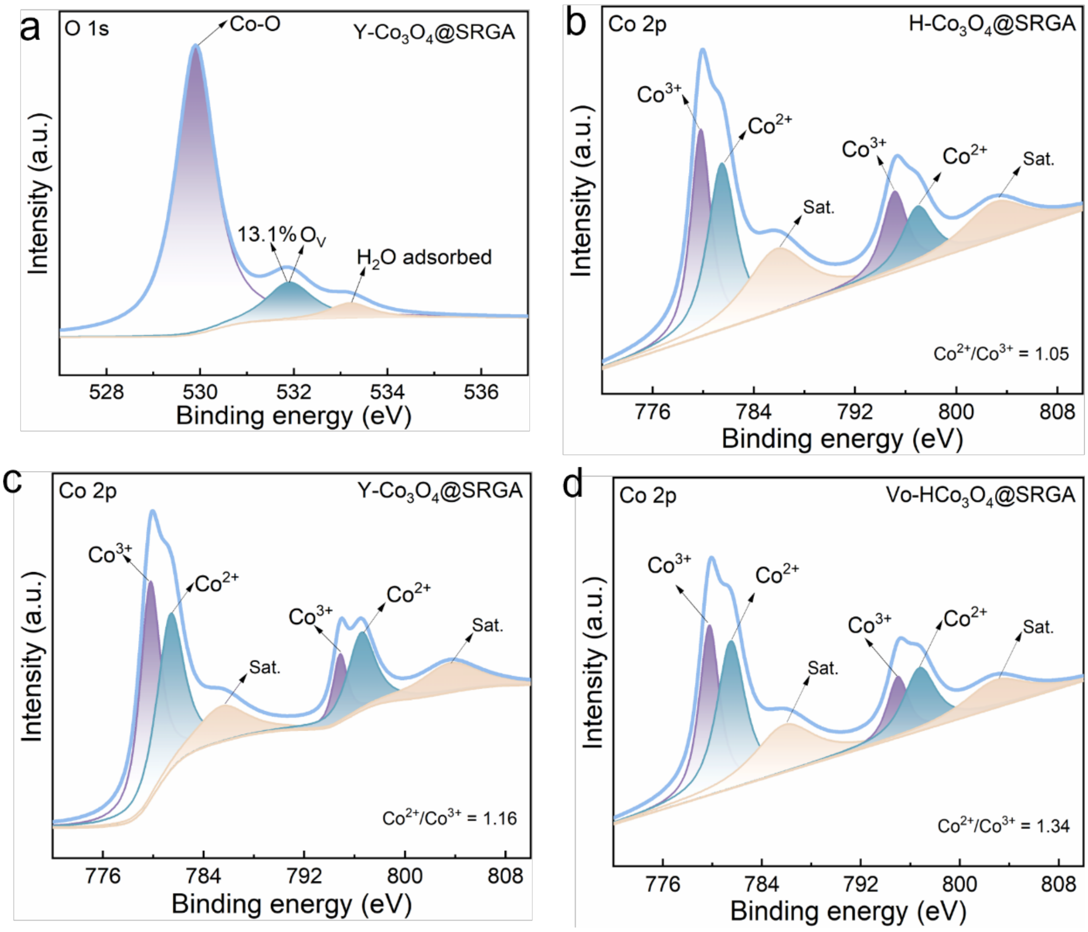

Figure S8. (a) high-resolution XPS of O1s of Y-Co_3O_4@SRGA. High-resolution XPS of Co 2p of (b) H-Co_3O_4@SRGA, (c) Y-Co_3O_4@SRGA, and (d) Vo-HCo_3O_4@SRGA.

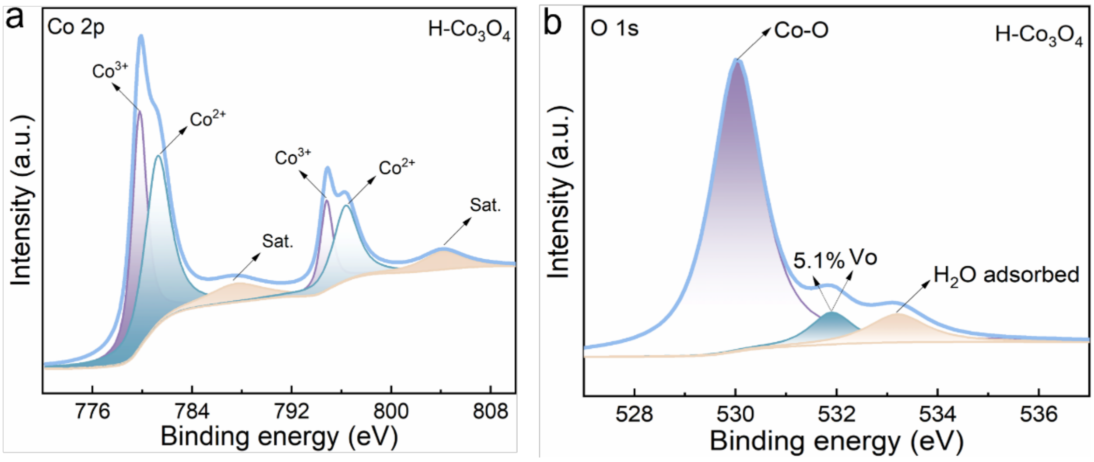

Figure S9. High-resolution XPS of (a) Co 2p and (b) O1s of H-Co$_3$O$_4$.

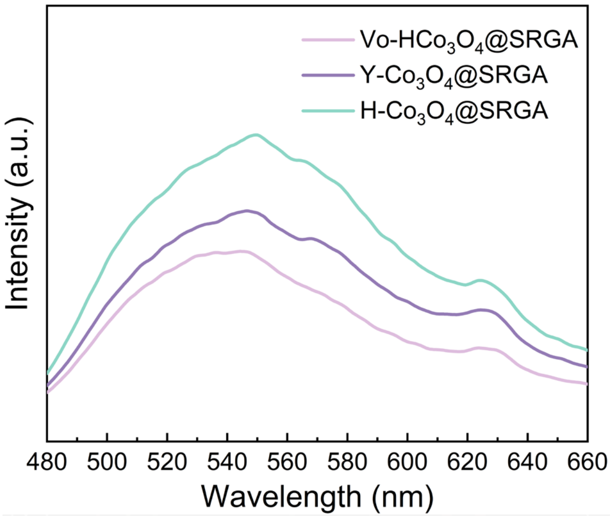

Figure S10. PL spectroscopy of H-Co$_3$O$_4$@SRGA, Y-Co$_3$O$_4$@SRGA, and Vo-HCo$_3$O$_4$@SRGA.

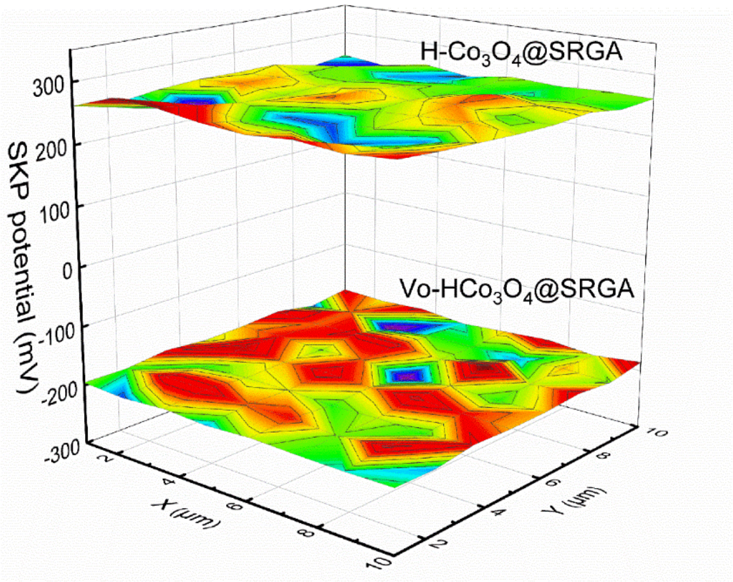

Figure S11. Work functions of H-Co$_3$O$_4$@SRGA and Vo-HCo$_3$O$_4$@SRGA.

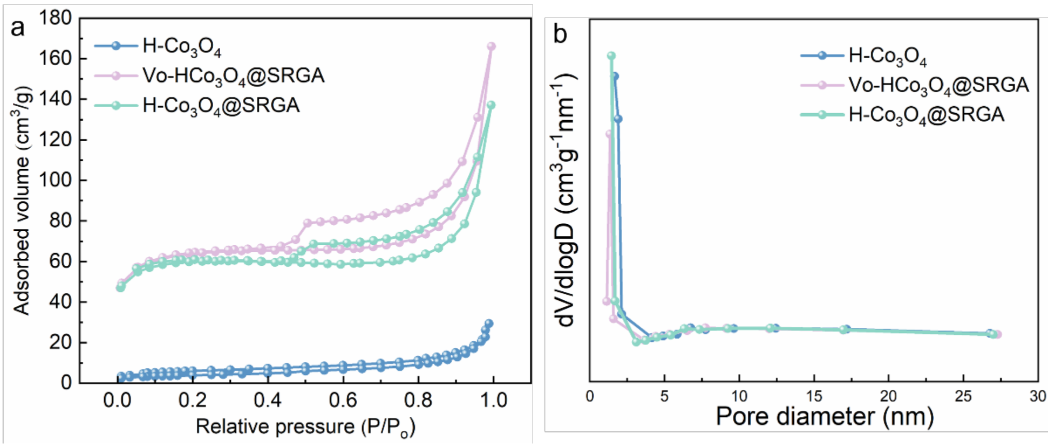

Figure S12. (a) N_2 adsorption-desorption isotherm and (b) pore size distribution curves of H-Co_3O_4, Vo-HCo_3O_4@SRGA, and H-Co_3O_4@SRGA.

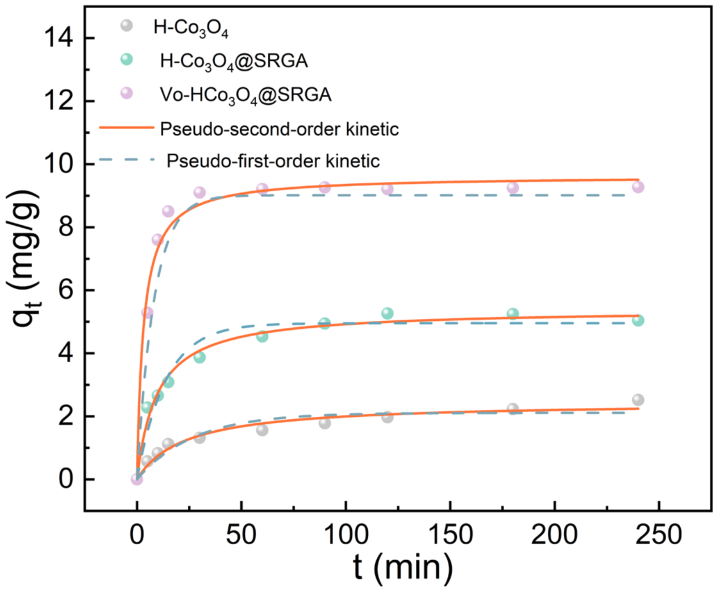

Figure S13. Adsorption kinetic for NO_3^- adsorption onto H-Co_3O_4, H-Co_3O_4@SRGA, and Vo-HCo_3O_4@SRGA.

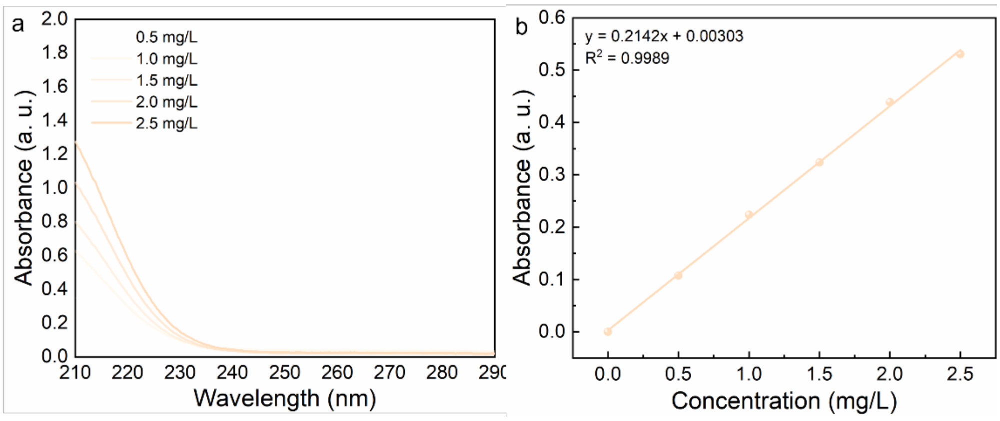

Figure S14. (a) UV-Vis curves and (b) corresponding calibration curve of indophenol assays with known NO_3^- concentrations.

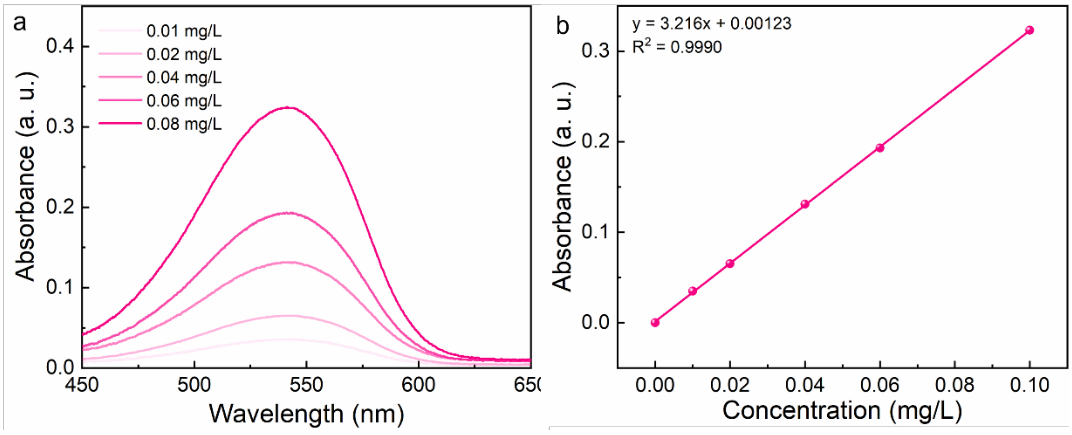

Figure S15. (a) UV-Vis curves and (b) corresponding calibration curve of indophenol assays with known NO_2^- concentrations.

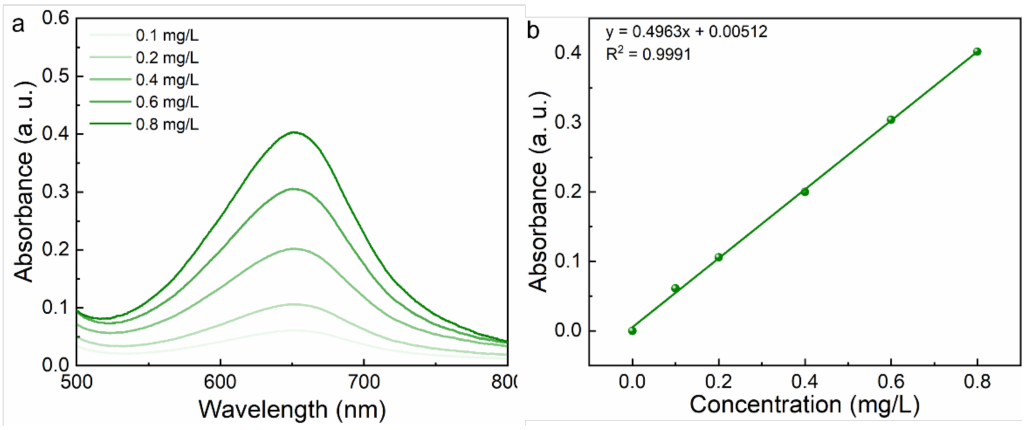

Figure S16. (a) UV-Vis curves and (b) corresponding calibration curve of indophenol assays with known NH_3 concentrations.

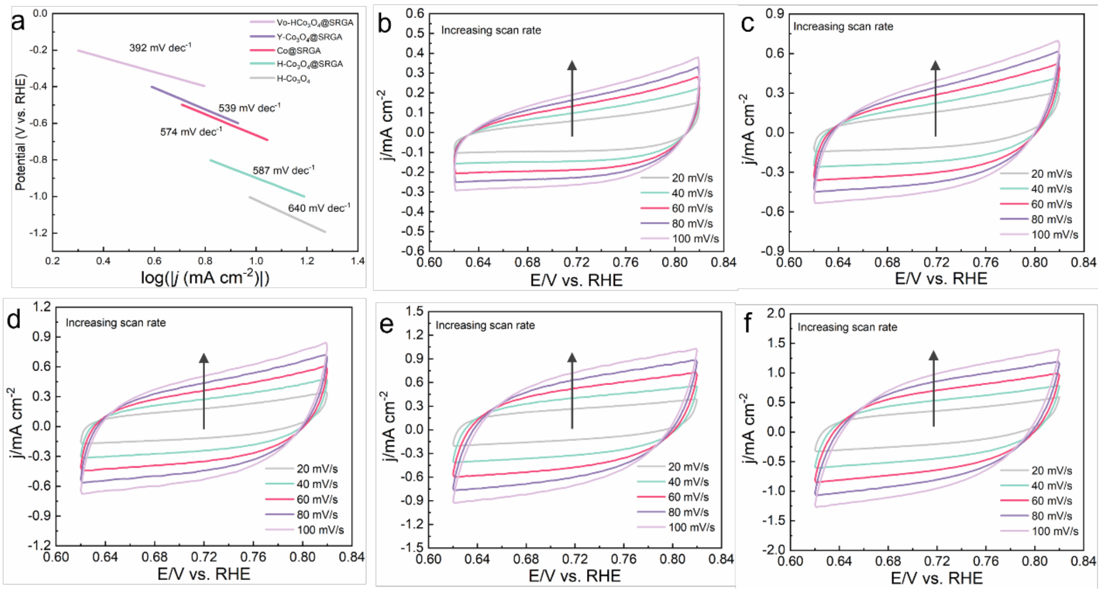

Figure S17. (a) Tafel slopes of H-Co_3O_4, H-Co_3O_4@SRGA, Co@SRGA, Y-Co_3O_4@SRGA, and Vo-HCo_3O_4@SRGA. CV measurements for testing the ECSAs of (b) H-Co_3O_4, (c) H-Co_3O_4@SRGA, (d) Co@SRGA, (e) Y-Co_3O_4@SRGA, and (f) Vo-HCo_3O_4@SRGA.

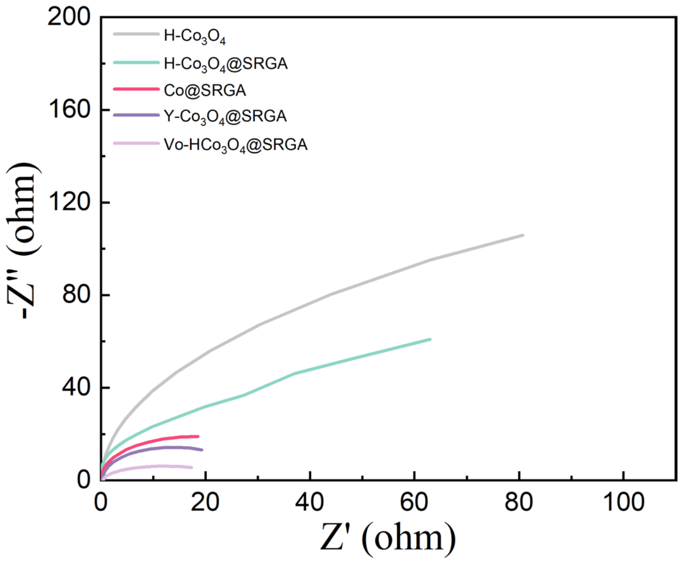

Figure S18. Nyquist plots for H-Co_3O_4, H-Co_3O_4@SRGA, Co@SRGA, Y-Co_3O_4@SRGA, and Vo-HCo_3O_4@SRGA.

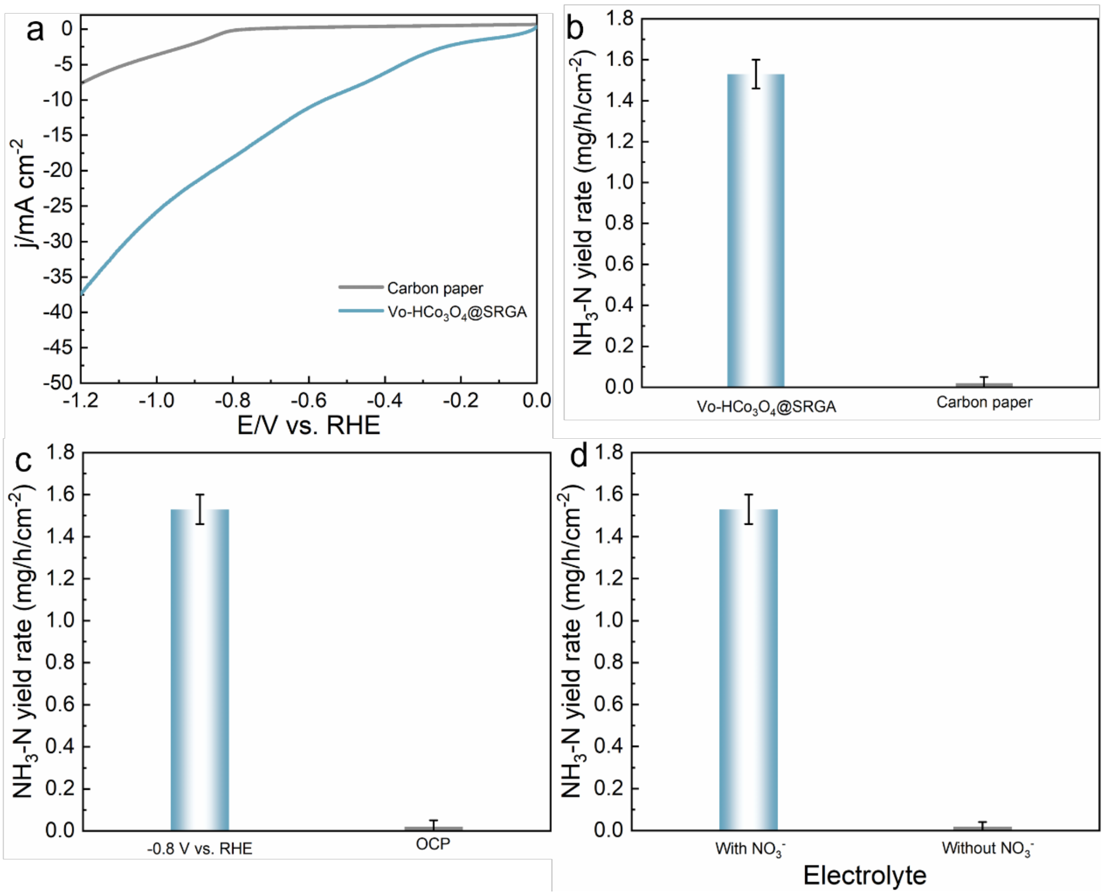

Figure S19. (a) LSV curves of carbon paper and Vo-HCo_3O_4@SRGA during the eNO_3^-RR process. (b) NH_3-N yield rates of carbon paper and Vo-HCo_3O_4@SRGA. (c) The comparation of NH_3-N yield rates of Vo-HCo_3O_4@SRGA at -0.8 V vs. RHE and open circuit potential (OCP). (d) The comparation of NH_3-N yield rates of Vo-HCo_3O_4@SRGA in the presence and without of NO_3^- electrolyte.

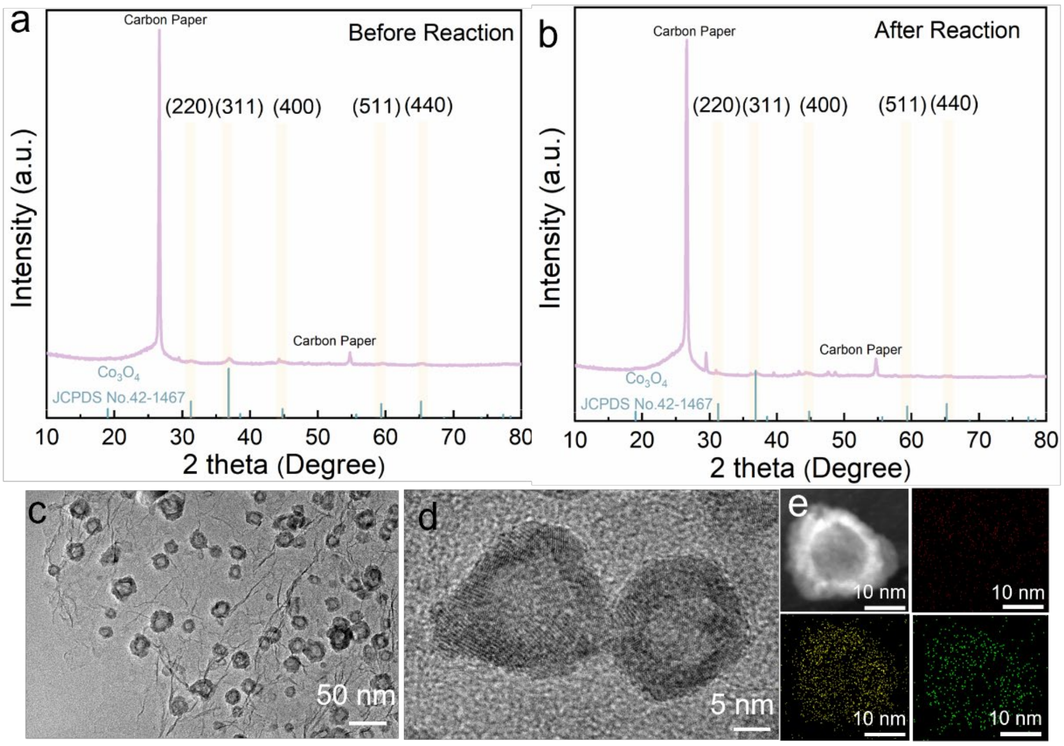

Figure S20. XRD patterns of Vo-HCo_3O_4@SRGA (a) before and (b) after eNO_3^-RR process. (c) TEM, (d) HRTEM, and (e) and elemental mappings of Vo-HCo_3O_4@SRGA after eNO_3^-RR process.

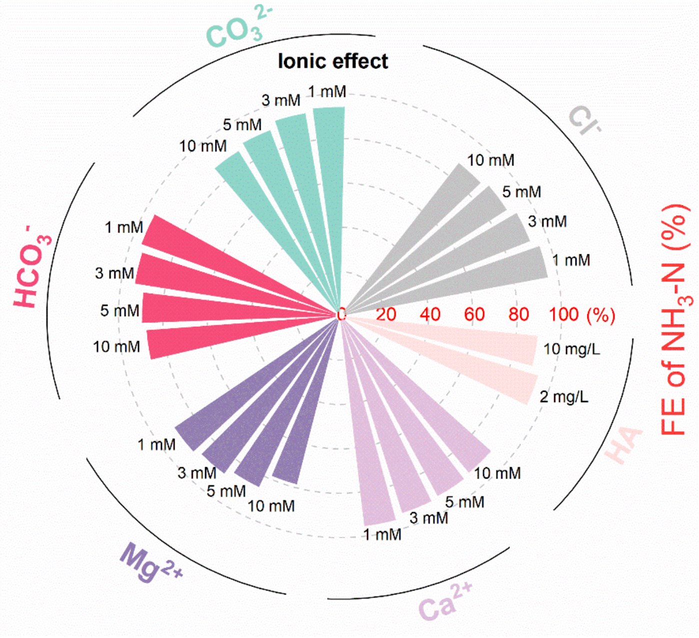

Figure S21. (a) Environmental interference factors on FE of NH_3-N over Vo-HCo_3O_4@SRGA.

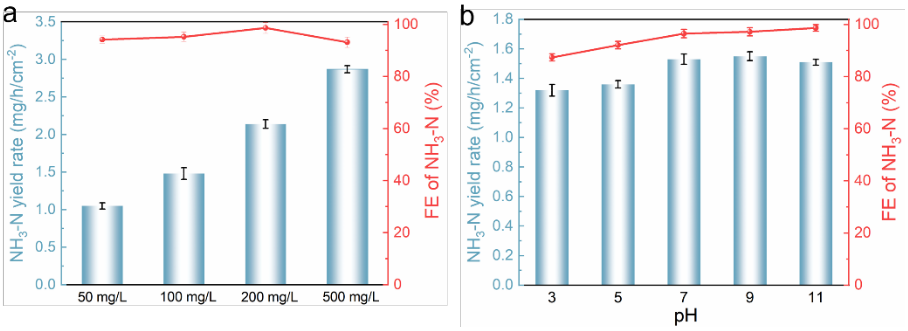

Figure S22. NH_3-N yield rates and FEs of Vo-HCo_3O_4@SRGA at (a) different NO_3^- concentrations and (b) different pH.

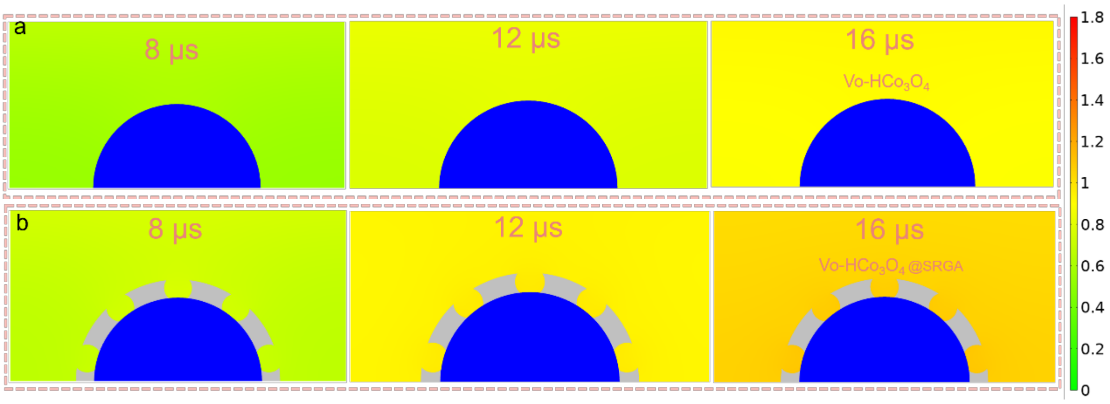

Figure S23. Simulated concentration distribution of NO_3^- on the surface of Vo-HCo_3O_4 and Vo-HCo_3O_4 encapsulated with SRGA at different diffusion time.

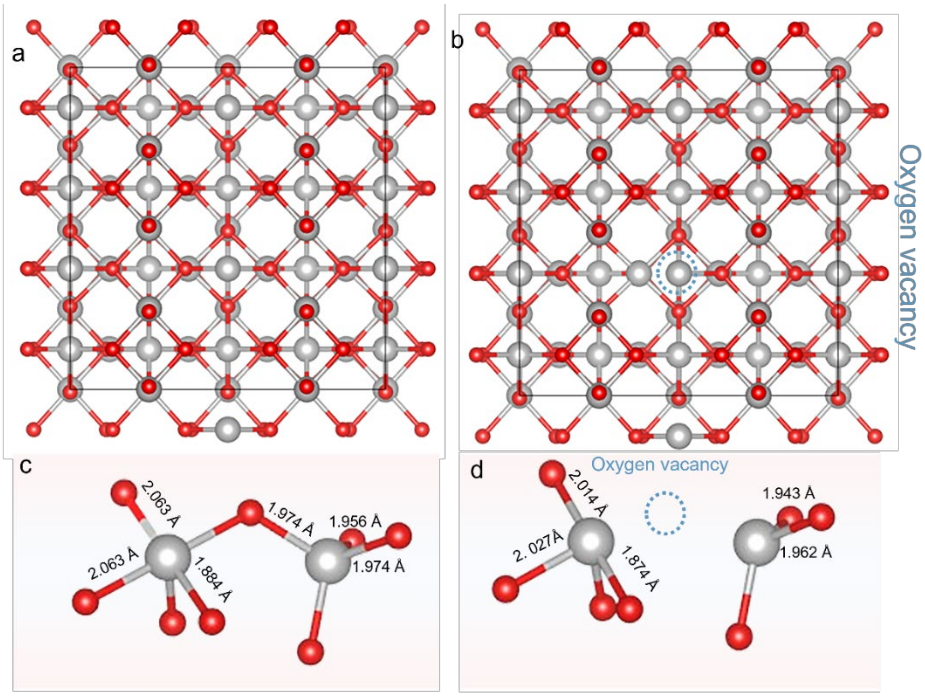

Figure S24. Structural models of (c) Co_3O_4 and (d) Vo-Co_3O_4 used in this work. Calculated Co-O bonds length of (c) Co_3O_4 and (d) Vo-Co_3O_4.

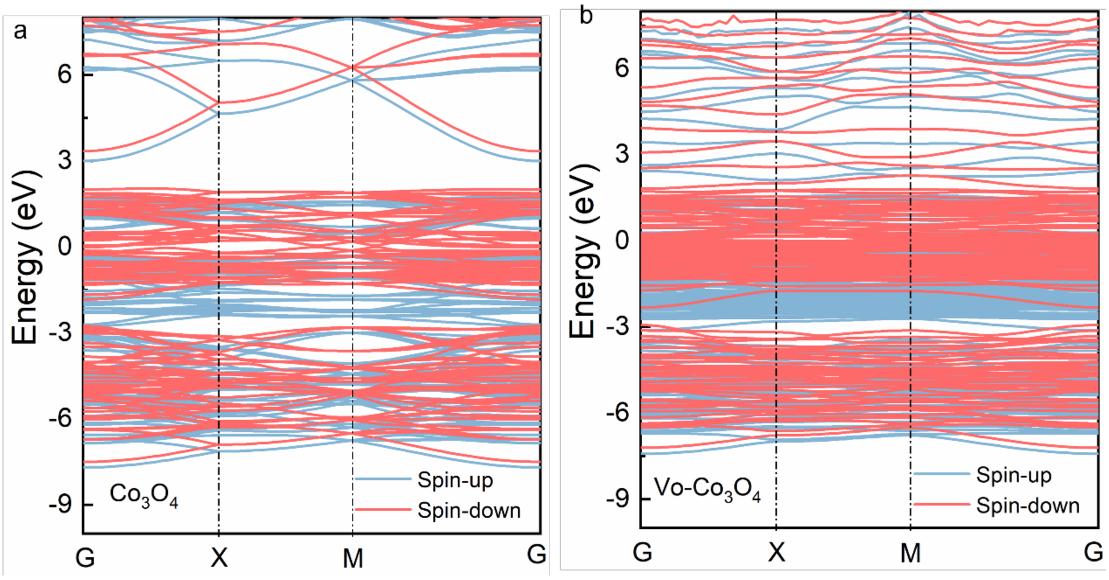

Figure S25. Calculated band structures of (a) Co_3O_4 and (b) Vo-Co_3O_4.

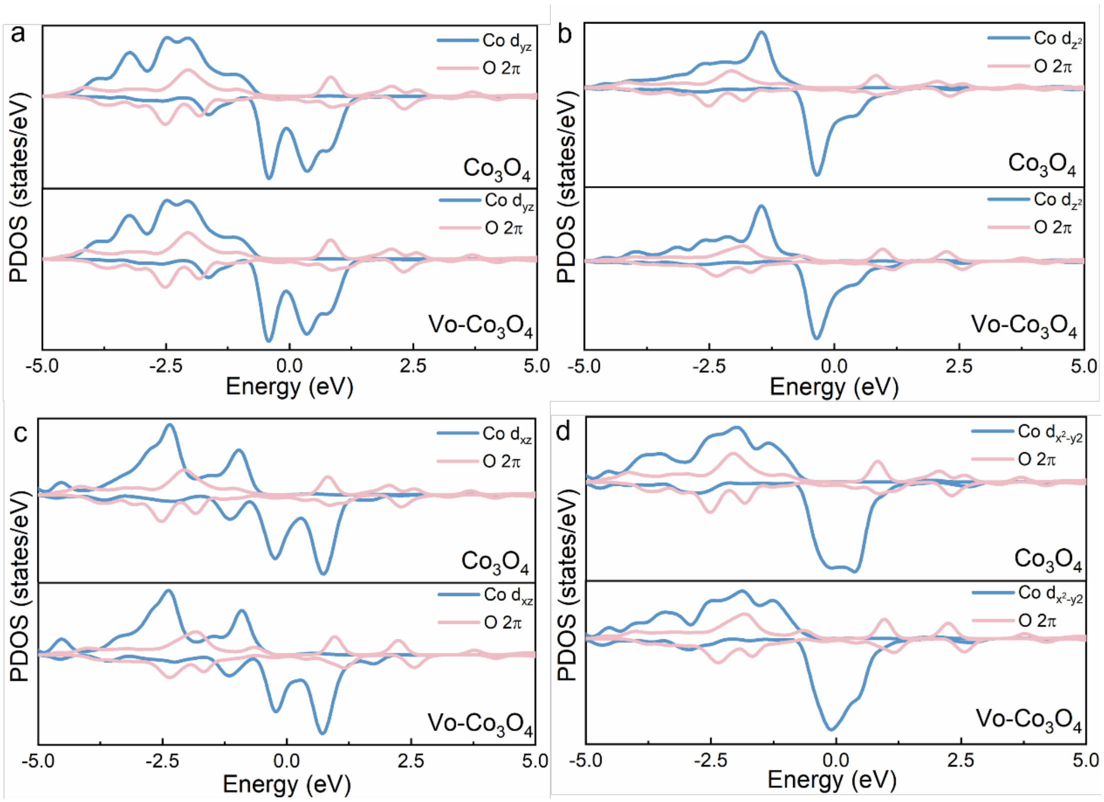

Figure S26. PDOS of (a) d_{yz}, (b) d_{z^2}, (c) d_{xz}, and (d) $d_{x^2\text{-}y^2}$ orbitals for NO_3^- adsorbed on Co_3O_4 and Vo-Co_3O_4.

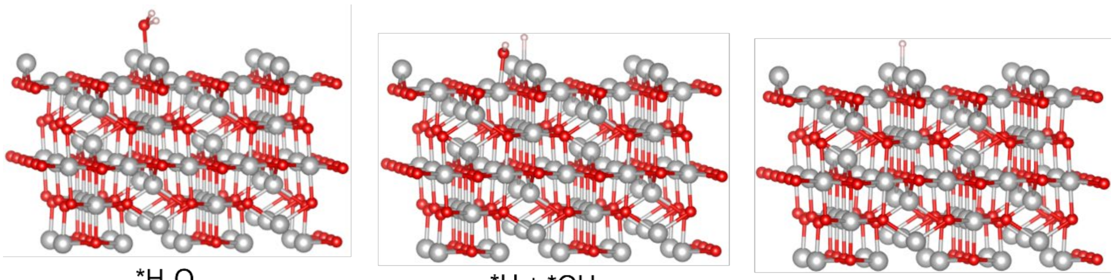

$*H_2O$ $*H + *OH$ $*H$

Figure S27. The tested adsorption geometries of $*H_2O$, $*H+*OH$ and $*H$ on the Co_3O_4 surface.

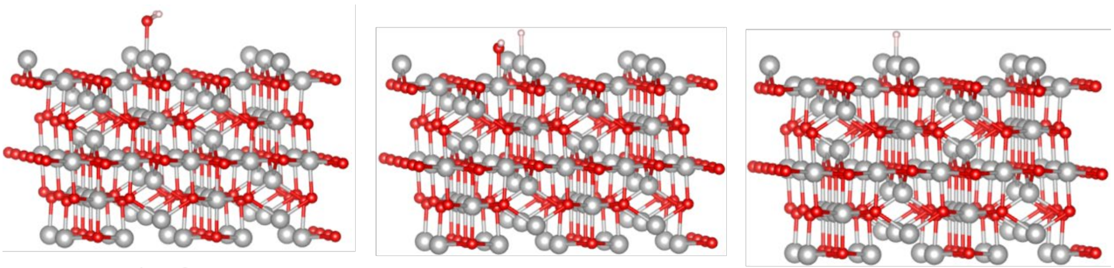

$^*H_2O$

*H + *OH

*H

Figure S28. The tested adsorption geometries of $^*H_2O$, *H+*OH and *H on the Vo-Co_3O_4 surface.

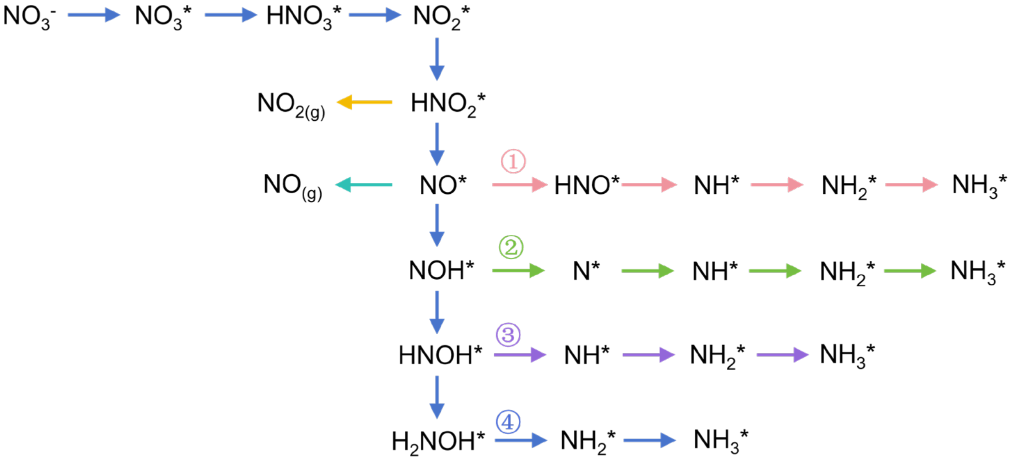

Figure S29. All possible reaction paths that result in NH_3 as the main product.

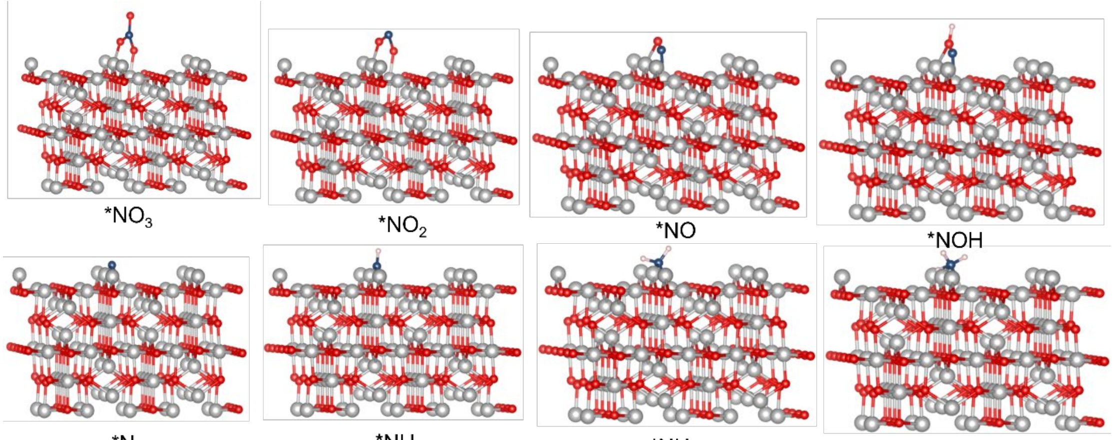

$*NO_3$ $*NO_2$ $*NO$ $*NOH$

$*N$ $*NH$ $*NH_2$ $*NH_3$

Figure S30. The tested adsorption geometries of $*NO_3$, $*NO_2$, $*NO$, $*NOH$, $*N$, $NH*$, $*NH_2$ and NH_3* on the Co_3O_4 surface.

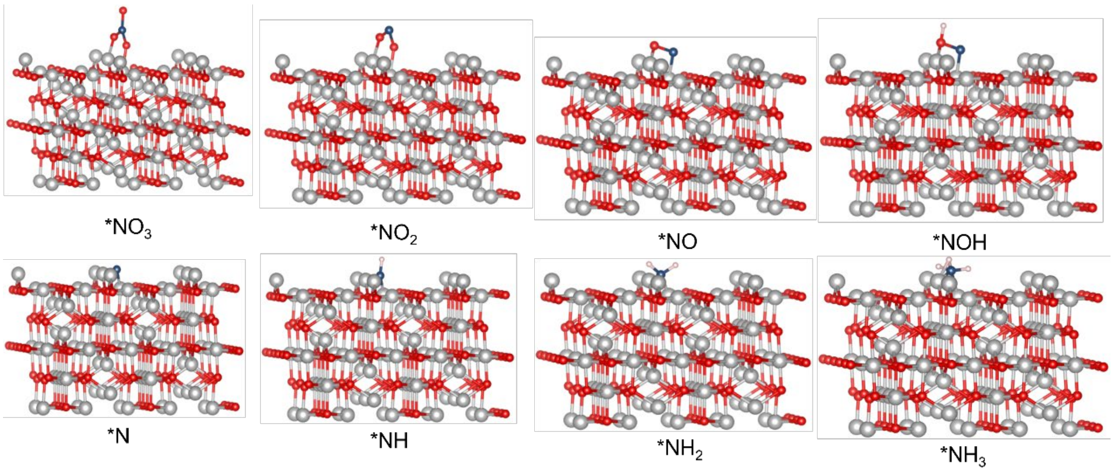

*NO_3 *NO_2 *NO *NOH

*N *NH *NH_2 *NH_3

Figure S31. The tested adsorption geometries of *NO_3, *NO_2, *NO, *NOH, *N, NH*, *NH_2 and NH_3* on the Vo-Co_3O_4 surface.

Table S1. The preparation details and mass loadings of Vo-HCo_3O_4@SRGA on carbon paper.

Samples name/μL Vo-HCo_3O_4@SRGA-X (X = 20-100 μL)	20	40	60	80	100
Active aera of carbon paper/cm^2			1		
Mass loading after pyrolysis/mg cm^{-2}	0.45	0.90	1.28	1.72	1.83

Table S2. Comparison of Vo-HCo_3O_4@SRGA with some related electrocatalysts in terms of materials used as well as preparation process.

Catalytic system	Use of Nafion solution or not	Use of precious metals or not	Use of high temperature heating or not	Use of Hazardous Chemicals Reagents or not	References
Vo-HCo_3O_4@SRGA	No	No	Yes (800 °C in Ar environment)	No	Our work
Pd-CoO_x	No	Yes (Pd)	No	Yes (HCl, acetone)	6
Mg single atom/carbon	Yes	No	Yes (850 °C in N_2 for 3 h)	Yes (acetone, hydrofluoric acid)	7
Cu-TiO_2	Yes	No	Yes (hydrothermal at 180 °C for 12 h, 600 °C in Ar for 2 h)	Yes (HCl)	8
Cu in an oxide octahedral molecular sieve (Cu(x)-OMS-1	Yes	No	Yes (hydrothermal at 140 °C for 24 h)	No	9
Mo-HATN-COFs	Yes	No	Yes (hydrothermal at 180 °C for 12 h)	Yes (H_2SO_4)	10
Fe_3C/NC	Yes	No	Yes (hydrothermal at 180 °C for 6 h, 700 °C in Ar for 2 h)	Yes (HCl)	11
NbO_x	Yes	No	Yes (hydrothermal at 180 °C for 12 h, 500 °C in Air for 4 h)	Yes ($H_2C_2O_4$, methanol)	12
Cu_2O/Cu@PdCu	Yes	Yes (Pd)	No	Yes (HCl)	13
Co_9S_8	Yes	No	Yes (450 °C in Ar/H_2 for 3 h)	Yes (methanol)	14
RhCu nanocavities	Yes	Yes (Rh)	Yes (350 °C in Ar/H_2 for 3 h)	Yes (dimethyl formamide)	15
Ru-Co_3O_4	Yes	Yes (Ru)	Yes (hydrothermal at 100 °C for 6 h, hydrothermal at 120 °C for 12 h, 350 °C in Air for 3 h, 250 °C in Air for 2 h)	Yes (HCl)	16

CuPd/CuO	No	Yes (Pd)	Yes (hydrothermal at 90 °C for 14 h, 300 °C in Air for 2 h)	Yes (NaBH$_4$ solution)	17
RuCu DAs/NGA	Yes	Yes (Ru)	Yes (800 °C in N$_2$ for 2 h)	No	18
FeIr alloy	No	Yes (Ir)	Yes (hydrothermal at 180 °C for 12 h)	Yes (HCl)	19
Ag$_1$@Cu$_2$O	No	Yes (Ag)	Yes (200 °C in Ar/H$_2$ for 1 h)	Yes (HCl)	20
Fe-TiO$_2$	Yes	No	Yes (800 °C in Air for 20 h, 800 °C in Air for 20 h)	Yes (HCl, Cs$_2$CO$_3$, TBAOH)	21
IrCu$_4$ alloy	Yes	Yes (Ir)	Yes (oil bath at 260 °C for 5 h)	Yes (cyclohexane)	22
Cu-SrRuO$_3$	Yes	Yes (Ru)	Yes (500 °C in Air for 6 h, 950 °C in Air for 12 h)	Yes (HNO$_3$)	23
FeSe$_2$/Fe$_3$O$_4$	No	No	Yes (hydrothermal at 180 °C for 24 h)	Yes (HCl, acetone)	24
Ru-B-Co$_3$O$_4$/CNT	Yes	Yes (Ru)	Yes (350 °C in Air for 3 h)	Yes (HNO$_3$)	25
Ru$_{SACs}$-CF	No	Yes (Ru)	No	Yes (HCl)	26
Ru/WO$_{3-x}$	No	Yes (Ru)	Yes (hydrothermal at 170 °C for 10 h, 350 °C in Ar/H$_2$ for 2 h, 250 °C in Ar/H$_2$ for 2 h))	Yes (HCl, acetone)	27
Ru$_{SA}$@Cu$_{2+1}$O	Yes	Yes (Ru)	Yes (300 °C in N$_2$ for 3 h)	Yes (NaBH$_4$ solution)	28
Rh$_1$-TiO$_2$	No	Yes (Rh)	Yes (400 °C in Air for 3 h)	Yes (Methyl methacrylate)	29
P-CoMoO$_4$-x nanowires	Yes	No	Yes (hydrothermal at 150 °C for 10 h, 400 °C in Ar for 2 h)	Yes (NH$_4$F solution)	30
IrCo alloy	Yes	Yes (Ir)	Yes (900 °C in N$_2$ for 2 h)	No	31
Ni-MOF-Ru rod qrray	No	Yes (Ru)	Yes (hydrothermal at 150 °C for 20 h)	Yes (HCl, acetone, C$_8$H$_6$O$_4$)	32
Co–B/Ru$_{12}$	Yes	Yes (Ru)	No	Yes (NaBH$_4$ solution)	33
Cu$_{11}$Ag$_3$ nanotips	No	Yes (Ag)	No	Yes (H$_2$SO$_4$)	34

Ni-MoS$_2$ nanosheets	Yes	No	Yes (hydrothermal at 180 °C for 20 h, 400 °C in Ar for 2 h)	Yes (thioacetamide)	35
HPdCuCo/RGO	Yes	Yes (Pd)	Yes (hydrothermal at 160 °C for 7 h)	No	36

Table S3. The specific surface areas, pore sizes and pore volumes of Vo-HCo_3O_4, HCo_3O_4@SRGA and Vo-HCo_3O_4@SRGA.

Samples	**Surface area (m^2 g^{-1})**	**Pore size (nm)**
H-Co_3O_4	9.5	4.3
H-Co_3O_4@SRGA	206.4	3.9
Vo-HCo_3O_4@SRGA	191.3	4.1

Table S4. Parameters of Pseudo-first-order and Pseudo-second-order kinetic models for NO_3^- adsorption by H-Co_3O_4, H-Co_3O_4@SRGA, and Vo-HCo_3O_4@SRGA.

Models	Parameters	H-Co_3O_4	H-Co_3O_4@SRGA	Vo-HCo_3O_4@SRGA
Pseudo-first-order	q_e (mg/g)	2.11	4.95	9.01
	K_1 (min^{-1})	0.037	0.073	0.12
	R^2	0.8978	0.9464	0.9416
Pseudo-second-order	q_e (mg/g)	2.25	5.40	9.63
	K_2 (g/(mg·min))	0.01	0.019	0.03
	R^2	0.9753	0.9822	0.9853

Table S5. Comparison of electrocatalytic eNO_3^-RR performance for Vo-HCo_3O_4@SRGA with some related electrocatalysts under low concentrations NO_3^- conditions.

Electrocatalyst	Electrolyte	Conditions	Performance	Reference
Vo-HCo_3O_4@SRGA	140 mg/L NO_3^--N+0.1 M Na_2SO_4	-0.8 V *vs.* RHE	$FENH_3$-N: 96.5% YNH_3-N: 1.53 mg h^{-1} cm^{-2}	**this work**
CoP	140 mg/L NO_3^--N+0.1 M Na_2SO_4 140 ppm NO_3^--N+0.1 M Na_2SO_4	-2.4 V *vs.* SHE -2.4 V *vs.* SHE	$FENH_3$-N: 38% YNH_3-N: 1.28 mg h^{-1} cm^{-2} $FENH_3$-N: 38% YNH_3-N: 1.275 mg h^{-1} cm^{-2}	[37]
CuCl/TiO_2	100 mg/L NO_3^--N+0.5 M Na_2SO_4	-1.0 V *vs.* RHE	$FENH_3$-N: 44.7% YNH_3-N: 1.50 mg h^{-1} cm^{-2}	[38]
CuSAs/NC	50 mg/L NO_3^--N+0.05 M Na_2SO_4	-1.06 V *vs.* SCE	$FENH_3$-N: 46.7% YNH_3-N: 0.482 mg h^{-1} cm^{-2}	[39]
Cu@C	14 ppm NO_3^--N+1 M KOH	-0.3 V *vs.* RHE	$FENH_3$-N: 72% YNH_3-N: 0.255 mg h^{-1} cm^{-2}	[40]
Cu@$CuCoO_2$	100 mg/L NO_3^--N+0.1 M Na_2SO_4	-0.44 V *vs.* RHE	$FENH_3$-N: 74.1% YNH_3-N: 0.204 mg h^{-1} cm^{-2}	[41]
$CuCoO_x$	50 ppm NO_3^--N+0.5 M Na_2SO_4	-1.1 V *vs.* SCE	$FENH_3$-N: 81% YNH_3-N: 0.288 mg h^{-1} cm^{-2}	[42]
Co/NC-800	100 ppm NO_3^--N+0.1 M Na_2SO_4	-1.2 V *vs.* Ag/AgCl	$FENH_3$-N: 81.2% YNH_3-N: 0.611 mg h^{-1} cm^{-2}	[43]
TiO_{2-x}	50 ppm NO_3^--N+0.5 M Na_2SO_4	-0.95 V *vs.* RHE	$FENH_3$-N: 85% YNH_3-N: 0.63 mg h^{-1} cm^{-2}	[44]
Cu-PTCAD	112.9 ppm NO_3^--N+0.1 M PBS (pH =7)	-0.4 V vs. RHE	$FENH_3$-N: 85.9% YNH_3-N: 0.362 mg h^{-1} cm^{-2}	[45]
NiPc-CNT	50 ppm NO_3^--N+0.05 M Na_2SO_4	-1.2 V *vs.* Ag/AgCl	$FENH_3$-N: 86.8% YNH_3-N: 0.156 mg h^{-1} cm^{-2}	[46]
Co-B@CoO_x	100 ppm NO_3^--N+0.5 M Na_2SO_4	-0.75 V *vs.* RHE	$FENH_3$-N: 86.82% YNH_3-N: 0.791 mg h^{-1} cm^{-2}	[47]
Cu@Cu_{2+1}O NWs	50 ppm NO_3^--N+0.5 M K_2SO_4	-1.2 V *vs.* SCE	$FENH_3$-N: 87.07% YNH_3-N: 0.469 mg h^{-1} cm^{-2}	[48]

Mn-O-C	100 ppm NO_3^--N+0.1 M K_2SO_4	-0.5 V *vs.* RHE	FENH$_3$-N: 89.0 ± 3.8% YNH$_3$-N: 0.796 mg h^{-1} cm^{-2}	[49]
$Cu_{1.5}$/NTC	50 ppm NO_3^--N+0.5 M Na_2SO_4	-0.75 V *vs.* RHE	FENH$_3$-N: 94.3% YNH$_3$-N: 0.618 mg h^{-1} cm^{-2}	[50]
Ni_3Fe-CO_3 LDH/Cu	70 ppm NO_3^--N+1 M KOH	-0.2 V *vs.* RHE	FENH$_3$-N: 96.8% YNH$_3$-N: 1.038 mg h^{-1} cm^{-2}	[51]

References

[1] K. Wang, S. Zhang, R. Wang, Y. Liu, G. Cao, X. Duan and S.-H. Ho, *Sep. Pur. Technol.*, 2022, **290**, 120862.

[2] P. E. Blöchl, *Phys. Re.v B Condens. Matter.*, 1994, ***50***, 17953.

[3] S. Grimme, *J. Comput. Chem.*, 2006, **27**, 1787-1799.

[4] G. Kresse and J. Furthmüller, *Comp. Mater. Sci.*, 1996, **6**, 15-50.

[5] J. P. Perdew, K. Burke and M. Ernzerhof, *Phys. Rev. Lett.*, 1996, **77**, 3865.

[6] Y. Wang, Y. Zeng, J. Xie, C. Wang, C. Zhou, L. Song, K. Ma and H. Yue, *Green Chem.*, 2025, **27**, 1763-1770.

[7] K. Kumar, P. Tripathi, G. Raj, D. Kalyan, D.B. Gorle, N.G. Mohan, S.K. Makineni, K. Ramanujam, A.K. Singh and K.K. Nanda, *Green Chem.*, 2024, **26**, 7931-7943.

[8] W.P. Utomo, H. Wu, R. Liu and Y.H. Ng, Green Chem., 2024, **26**, 1443-1453.

[9] S. Li, C. Xiao, R. Chen, M. Wang, Y. Ma, K. Luo, M. Shen, Y. Zhu, Y. Li and C. Li, *Green Chem.*, 2023, **25**, 10549-10555.

[10] H. Huang and K. Wang, *Green Chem.*, 2023, **25**, 9167-9174.

[11] Y. Wang, L. Zhang, Y. Niu, D. Fang, J. Wang, Q. Su and C. Wang, *Green Chem.*, 2021, **23**, 7594-7608.

[12] X. Wan, W. Guo, X. Dong, H. Wu, X. Sun, M. Chu, S. Han, J. Zhai, W. Xia, S. Jia, M. He and B. Han, *Green Chem.*, 2022, **24**, 1090-1095.

[13] L. Sun, X. Min, J. Wang, Y. Yang, S. Han, D. Fan, Y. Jing, D. Xu, W. Wang and B. Liu, *Adv. Mater.*, 2025, 2503291.

[14] J. Zhang, J. Li, W. Chen, Q. Zhang, J. Li, Y. Li, X. Ren, X. Ouyang, X. Meng, J. Qiu, J. Hu, S. Ye, J. Liu and Q. Zhang, *Appl. Catal. B-Environ. Energy*, 2025, **373**, 125333.

[15] L. Zhu, H. Yao, L. Sun, L. Ai, H. Zhai and C. Yi, *Small*, 2025, 2502787.

[16] J. Jiang, L. Zhang, G. Wu, J. Zhang, Y. Yang, W. He, J. Zhu, J. Zhang and Q. Qin, *Angew. Chem. Int. Edit.*, 2025, e202421240.

[17] J. Li, L. Liu, S. Huang, H. Wang, Y. Tang, C. Zhang, F. Du, R. Ma, C. Li and C. Guo, *Adv. Funct. Mater.*, 2025, 2501527.

[18] K. Liu, Z. Sun, X. Peng, X. Liu, X. Zhang, B. Zhou, K. Yu, Z. Chen, Q. Zhou, F. Zhang, Y. Wang, X. Gao, W. Chen and P. Chen, *Nat. Commun.*, 2025, **16**, 2167.

[19] J. Xiong, L. Jiang, B. Zhu, S. Huang, S. Wu, K. You, X. Li and L. Feng, *Adv. Funct. Mater.*, 2025, 23705.

[20] L. Zhang, Y. Cai, Y. Li, C. Sun, Y. Xiao, Y. Yang, D. Chen, D. Xiao, C.-F. Lee, Y. Wang, S. Feng, H.-T. Wang, Y.-C. Shao, T.-S. Chan, H. Ishii, N. Hiraoka, X. Wang, J. Luo and L. Han, *Energ. Environ. Sci.*, 2025, **18**, 2804-2816.

[21] J. Wang, K. Zhao, Y. Yao, F. Xue, F. Lu, W. Yan, F. Yuan and X. Wang, *Nat. Commun.*, 2025, **16**, 1129.

[22] N. He, Z. Yuan, C. Wu, S. Xi, J. Xiong, Y. Huang, G. Lian, Z. Du, L. Liu, D. Wu, Z. Chen, W. Tu, Z. Zou and S.-Y. Tong, *ACS Nano*, 2025, **19**, 4684-4693.

[23] L. Lv, H. Tan, Y. Liu, N. Li, Q. Ji, Y. Kong, H. Wang, M. Sun, M. Fan, C. Wang and W. Yan, *Adv. Funct. Mater.*, 2025, 2423612.

[24] Y. Du, H. Lu, J. Wu, Y. Zou, Z.-F. Huang, J.-J. Zou, T. Mu, J. Gao, X.-D. Zhu and Y.-C. Zhang, *Angew. Chem. Int. Edit.*, 2025, **64**, e202420903.

[25] X. Wang, L. Chen, Q. Wei, Z. Wen, G. Ding, Z. Feng, Z. Wang and Q. Jiang, *Chem. Eng. J.*, 2025, **504**, 158814.

[26] T. Xiang, X. Liu, Z. Wang, Y. Zeng, J. Deng, W. Xiong, M. Cheng, J. Liu, C. Zhou and Y. Yang, *Appl. Catal. B-Environ. Energy,* 2025, **365**, 124943.

[27] H. Fu, S. Lu, Y. Xin, S. Xiao, L. Chen, Y. Li and K. Shen, *Energ. Environ. Sci.*, 2025, **18**, 818-830.

[28] Y. Lin, Y. Wang, Y. Xu, H. Liu, X. Liu, L. Shan, C. Wu, L. Yang and L. Song, *Adv. Funct. Mater.*, 2025, **35**, 2417486.

[29] Z.L. Zhao, S. Yang, S. Wang, Z. Zhang, L. Zhao, Q. Wang and X. Zhang, *Adv. Sci.*, 2025, **12**, 2411705.

[30] Y. You, H. Chen, J. Guo, Z. Feng, J. Zhan, F. Yu and L.-H. Zhang, *Appl. Catal. B-Environ. Energy*, 2025, **363**, 124837.

[31] Y. Tang, P. Ran, L. Zhong, H. Liao, Q. Tong, W. Zou and L. Dong, *Chem. Eng. J.*, 2024, **500**, 157518.

[32] Y. Yao, X. Wei, H. Zhou, K. Wei, B. Kui, F. Wu, L. Chen, W. Wang, F. Dai, P. Gao, N. Wang and W. Ye, *ACS Catal.*, 2024, **14**, 16205-16213.

[33] J. Zhang, T. Quast, B. Eid, Y.-T. Chen, R. Zerdoumi, S. Dieckhöfer, J.R.C. Junqueira, S. Seisel and W. Schuhmann, *Nat. Commun.*, 2024, **15**, 8583.

[34] C. Wang, Z. Liu, Q. Peng, D. Xing, T. Hu, F. Du, C. Li, R. Ma, H. Yang and C. Guo, *Angew. Chem. Int. Edit.*, 2025, **64**, e202415259.

[35] J. Lv, X. Sun, F. Wang, R. Yang, T. Zhang, T. Liang, W. Rong, Q. Yang, W. Xue, L. Wang, X. Xu and Y. Liu, *Adv. Funct. Mater.*, 2024, **34**, 2411491.

[36] R. Yan, H. Yin, X. Zuo, W. Peng, X. Zhu, L. Shi, J. Hou, D. Wang, F. Ye, J. Li, B. Mao and C. Hu, *Appl. Catal. B-Environ. Energy*, 2025, **361**, 124609.

[37] J. Gao, N. Shi, X. Guo, Y. Li, X. Bi, Y. Qi, J. Guan and B. Jiang, *Environ. Sci. Technol.*, 2021, **55**, 10684-10694.

[38] W.-J. Sun, H.-Q. Ji, L.-X. Li, H.-Y. Zhang, Z.-K. Wang, J.-H. He and J.-M. Lu, *Angew. Chem. Int. Ed.*, 2021, **60**, 22933-22939.

[39] T. Zhu, Q. Chen, P. Liao, W. Duan, S. Liang, Z. Yan and C. Feng, *Small*, 2020, **16**, 2004526.

[40] Z. Song, Y. Liu, Y. Zhong, Q. Guo, J. Zeng and Z. Geng, *Adv. Mater.*, 2022, **34**, 2204306.

[41] Y. Xue, Q. Yu, J. Fang, Y. Jia, R. Wang and J. Fan, *Small*, 2024, **20**, 2400505.

[42] L. Fang, S. Wang, S. Lu, F. Yin, Y. Dai, L. Chang and H. Liu, *Chinese Chem. Lett.*, 2024, **35(4)**, 108864.

[43] H. Liu, J. Qin, J. Mu and B. Liu, *J. Colloid Interf. Sci.*, 2023, **636**, 134-140.

[44] R. Jia, Y. Wang, C. Wang, Y. Ling, Y. Yu and B. Zhang, *ACS Catal.*, 2020, **10(6)**, 3533-3540.

[45] G.-F. Chen, Y. Yuan, H. Jiang, S.-Y. Ren, L.-X. Ding, L. Ma, T. Wu, J. Lu and H. Wang, *Nat. Energy*, 2020, **5**, 605-613.

[46] Y. Li, L. Ren, Z. Li, T. Wang, Z. Wu and Z. Wang, *ACS Appl. Mater. Interfaces*, 2022, **14**, 53884-53892.

[47] X. Zhu, C. Ma, Y.-C. Wang, K. Qu, L. Song, J. Wang, Y. Gong, X. Liu, J. Zhang, Q. Lu and A.-L. Wang, *Energ. Environ. Sci.*, 2024, **17**, 2908-2920.

[48] T. Ren, K. Ren, M. Wang, M. Liu, Z. Wang, H. Wang, X. Li, L. Wang and Y. Xu, *Chem. Eng. J.*, 2021, **426**, 130759.

[49] S. Zhang, Y. Zha, Y. Ye, K. Li, Y. Lin, L. Zheng, G. Wang, Y. Zhang, H. Yin, T. Shi and H.

Zhang, *Nano-Micro Lett.*, 2023, **16**, 9.

[50] X.-Y. Ji, K. Sun, Z.-K. Liu, X. Liu, W. Dong, X. Zuo, R. Shao and J. Tao, *Nano-Micro Lett.*, 2023, **15**, 110.

[51] K.-H. Kim, H. Lee, X. Huang, J.H. Choi, C. Chen, J.K. Kang and D. O'Hare, *Energ. Environ. Sci.*, 2023, **16**, 663-672.